

Enhancing the Purity of Reflective Structural Colors with Ultrathin Bilayer Media as Effective Ideal Absorbers

Zhengmei Yang, Chengang Ji, Dong Liu, and L. Jay Guo*

Structural colors of high purity and brightness are desired in various applications. This study presents a general strategy of selecting the appropriate material and thickness of each layer to create high-purity reflective colors in a classic asymmetric Fabry–Pérot cavity structure based on a dielectric–absorber–dielectric–metal multilayered configuration. Guided by the derived complex refractive index of the ideal absorber layer, an effective absorbing bilayer medium consisting of two ultrathin lossy films is used to improve the color purity of reflective colors by suppressing the reflection of its complementary colors with the enhanced optical absorption. Highly pure red, green, and blue reflective colors are designed and experimentally demonstrated employing different effective bilayer absorbers. Due to the high refractive index of the dielectric material, the colored structures exhibit great angle-robust appearance (blue and red colors are up to $\pm 60^\circ$, and green color is up to $\pm 45^\circ$). The generalized design principles and the proposed method of using effective bilayer absorbers open up new avenues for realizing high-purity thin-film structural colors with more materials selections.

1. Introduction

Structural colors arising from resonant interactions between light and nanostructures have received increasing interest recently owing to their potential applications in various areas including color printing,^[1–6] display/imaging,^[7–9] optical decoration,^[10] solar cells,^[11–13] and so forth. In contrast to existing color filters exploiting chemical colorant pigments or organic dyes, structural color filters offer unique advantages

of nontoxicity, no-fading color, thin thickness, great scalability, high resolution, and easy tunability.^[14] To date, a large amount of research work discussed the generation of structural colors employing plasmon resonance,^[15,16] Mie resonance,^[17–19] or guided-mode resonance (GMR) based on sub-wavelength patterns.^[20,21] A wide color gamut is desired in many applications, and can be obtained by adjusting the structural dimensions of metal or all-dielectric nanostructures, such as duty cycle, shape, and height (thickness).^[22–24] However, plasmonic colors show poor quality factors and intensities due to the inherent loss of metals, resulting in the low color purity and brightness.^[25] GMR and Mie resonances can produce high-purity colors with full width at half-maximum (FWHM) of ≈ 12 and ≈ 30 nm, respectively, but their output colors are highly dependent on the angle and polarization state of incident light due to the momentum matching condition.^[26,27]

More importantly, these structures tend to be complicated and require 100 nm scale patterning, which are cost prohibitive for high volume and large-area applications.


Comparing to aforementioned color filters, planar thin-film structures based on Fabry–Pérot (F–P) cavity resonances can create wide-range colors by simply varying the spacer layer thickness. Their fabrication procedures only require physical vapor deposition tools (e.g., evaporation or sputtering systems), which have advantages of low cost and high scalability.^[28–30] In addition, great angle-insensitive performance can be achieved by using high-index materials or phase compensating overlayers.^[31,32] In particular, nontrivial reflection phase shift occurring at a semiconductor–metal interface allows for strong interference behaviors in ultrathin cavity layers, which has been used to generate various colors with improved angular insensitivity for both transverse magnetic (TM) and transverse electric (TE) polarizations.^[33] This recent study renewed the interest in interference color filters based on ultrathin absorbing films.^[34,35]

A wide variety of thin-film configurations have been proposed for achieving RGB (red, green and blue) transmissive colors and CMY (cyan, magenta and yellow) reflective colors employing constructive and destructive interferences, respectively.^[36–38] It is typically difficult to generate high-purity reflective RGB colors due to the narrow absorption bandwidth caused by the cavity resonances.^[28] In recent years, many efforts have been made to design distinctive RGB reflective colors using thin-film structures.^[30,39,40] For example, Yang et al. achieved three

Dr. Z. Yang, Dr. C. Ji, Prof. L. J. Guo
Department of Electrical Engineering and Computer Science
University of Michigan
Ann Arbor, MI 48109, USA
E-mail: guo@umich.edu

Dr. Z. Yang
School of Physics and Electronics
State Key Laboratory of Advanced Design and Manufacturing
for Vehicle Body
Hunan University
Changsha 410082, China

Dr. D. Liu
MIIT Key Laboratory of Thermal Control of Electronic Equipment
School of Energy and Power Engineering
Nanjing University of Science and Technology
Nanjing 210094, China

 The ORCID identification number(s) for the author(s) of this article can be found under <https://doi.org/10.1002/adom.201900739>.

DOI: 10.1002/adom.201900739

primary RGB reflective color filters with high angle insensitivity by optimizing the thickness of each layer in the asymmetric F–P cavities comprised of a titanium dioxide (TiO₂) anti-reflection (AR) overlayer, a thin absorptive layer of chromium, an amorphous silicon (a-Si) spacer layer, and a silver (Ag) mirror from top to bottom.^[40] Similar structures using a compound semiconductor (zinc sulfide (ZnS)) to replace a-Si have been presented in a US patent application.^[41] However, the underlying principle was not sufficiently discussed. It is noteworthy that the color purity and brightness of devices in ref. [40] are limited due to both the high loss of the cavity material and the inadequate absorption at the unwanted wavelengths. Hong et al. demonstrated a single mirror interferometric display technology by utilizing microelectronic mechanical system actuation devices to control the spacer layer thickness in real time.^[7] Although the obtained RGB reflective color filters exhibit fairly high color purity (FWHM of ≈70 nm) and brightness (the maximum reflectivity over 85%), multilayer dielectric coatings (a total of eight thin films in their structures) are required to enhance the absorption of nontargeted colors, which makes the design and fabrication process complicated. Therefore, how to achieve vivid, highly saturated RGB reflective colors with simpler thin-film structures still remains challenging.

In this work, we present general design principles of a classic and simple dielectric–absorber–dielectric–metal (DADM) film structure to elucidate the material and thickness selection

of each layer in order to produce high-purity RGB reflective colors. In particular, an effective absorbing bilayer medium consisting of two ultrathin lossy films is designed to satisfy the derived complex refractive index for the ideal absorber layer, which enhances the off-peak optical absorption over a broad wavelength range, leading to saturated colors with high peak reflections. This strategy provides an additional freedom to enhance the color purity of thin-film reflective colors and a great flexibility to select various material combinations. We demonstrate both theoretically and experimentally that highly saturated RGB reflective colors can be achieved by adjusting the thicknesses of dielectric layers and selecting different effective bilayer absorbers. Besides, these devices exhibit great angular tolerance (blue and red colors are up to ±60° and green color is up to ±45°) attributed by the high refractive indices of constituent materials. The excellent performance and low fabrication cost of high-reflectance RGB colors proposed here enable their potential applications in various areas including decorations, colored display/imaging, light emitting diodes, and so on.

2. Design Principle and Results

First, we present a general guiding principle on how to choose the material and thickness of each layer in a representative DADM thin-film structure illustrated in Figure 1a,

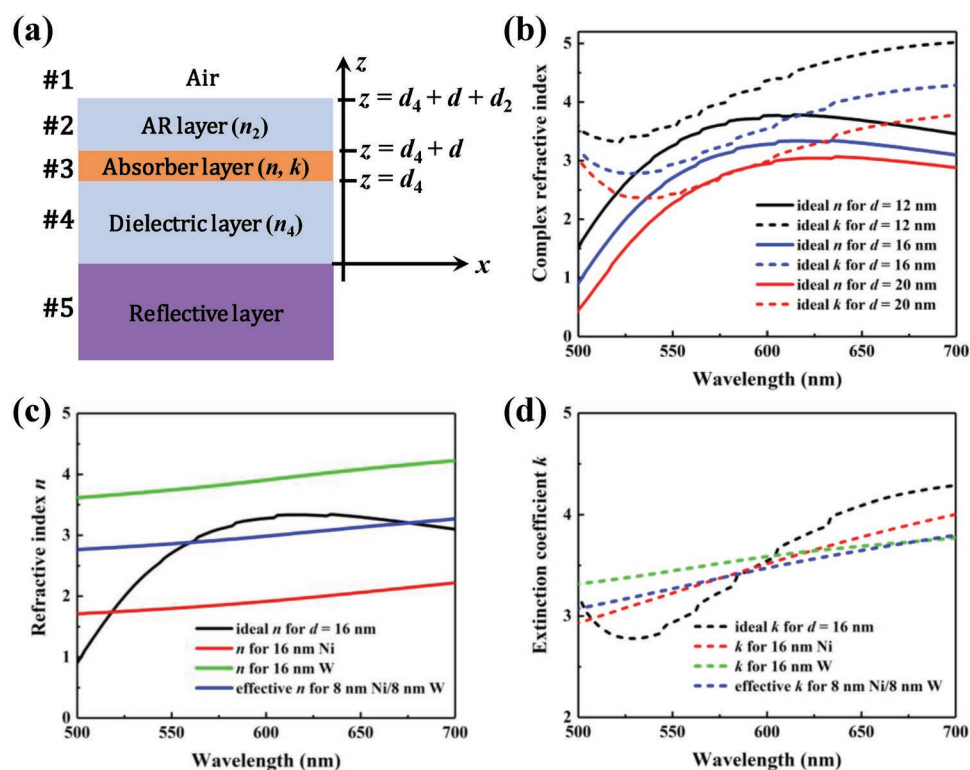


Figure 1. a) A schematic diagram of a common DADM thin-film structure to achieve high-purity RGB reflective color filters. It consists of a reflective layer with optical thickness, a dielectric layer (refractive index n_4 and thickness d_4), an absorber layer (refractive index n , extinction coefficient k , and thickness d), and an anti-reflection (AR) layer (refractive index n_2 and thickness d_2) from bottom to top. b) The calculated ideal complex refractive indices (n, k) of the absorber layer at wavelengths from 500 to 700 nm for producing high-purity blue color filters when the thickness d is fixed to be 12, 16, and 20 nm, respectively. c) The refractive indices and d) extinction coefficients comparisons between ideal absorber material, single metal Ni, W, and the Ni/W bilayer film in the case of $d = 16$ nm for the blue color filter.

to produce RGB reflective color filters with high color purity and brightness. It is a classic asymmetric F–P resonator, in which strong interference effects occurring in top and middle dielectric materials result in the selective reflection of the incident light at the peak reflection wavelength, and strong optical absorption by the absorber layer at off-peak wavelengths. Now we explain the physics of this structure. The bottom reflective layer is used to provide high reflection and prevent any light transmission. Therefore, it should be a sufficiently thick metal layer with high reflectivity across the entire visible spectrum, and the material of choice can be selected from a group comprising aluminum (Al) and Ag. To achieve high-purity reflective color, the ideal reflection spectrum should feature high reflectivity within the wavelength range of the target color and perfect absorption at other wavelengths within the visible band. According to the light absorption of the absorber layer: $A(z, \lambda) = \frac{2\pi c \epsilon_0 n k}{\lambda} |E(z, \lambda)|^2$, where c is the speed of light, ϵ_0 is the permittivity of free space, $E(z, \lambda)$ is the electric field intensity of the incident wavelength λ in the absorber layer, and n and k are the refractive index and extinction coefficient of the absorber layer, respectively. At the peak reflection wavelength λ_c , the absorber layer should be placed at the position where $E(\lambda_c) \approx 0$ to minimize absorption loss and achieve high reflectivity. Thus, the thickness of the middle dielectric layer should be $d_4 = \frac{\lambda_c}{2n_4}$, assuming the bottom reflective layer is a perfect electric conductor for simplicity.^[7] Moreover, to increase the contrast, the top AR layer is usually employed to reduce reflection in the off-peak region by introducing an additional resonant cavity. The thickness d_2 of the AR layer is determined by $\frac{\lambda_0}{4n_2}$, where λ_0 is the target wavelength where the reflection is suppressed. At the same time, the dielectric materials with high refractive indices (n_2 and n_4) should be adopted as the AR layer and the spacer layer to improve the angle insensitivity of the designed color filters.^[42]

The material and thickness selections of the absorber layer are most crucial for designing ideal reflective colors. The absorber layer should be much thinner than the wavelength to avoid intrinsic absorption in this layer at λ_c , so the electric field intensity in this layer can be approximated to be constant. Resultantly, the electric field intensities at the 2–3 interface ($E(z = d_4 + d)$) and the 3–4 interface ($E(z = d_4)$) can both be approximated to zero since the absorber layer is placed at the position where $E(\lambda_c) \approx 0$ to achieve high reflectivity. Based on these two conditions, we can deduce that the thickness d of the absorber layer should be less than $\frac{\lambda_c}{4\pi n}$, where n is the refractive index of the absorber layer (see more details in the Supporting Information). On the other hand, d cannot be too small; otherwise the absorption efficiency will be very low at off-peak reflection wavelengths. The high reflectivity within the wavelength region of the target color can be guaranteed when d falls into this thickness range. In order to achieve perfect absorption at the off-peak reflection wavelengths, the ideal complex refractive index of the absorber layer at normal incidence can be calculated when the thickness and material of other layers are known. The design of blue reflective color is taken as an

example to elucidate the design principle of high-purity reflective colors. A 100 nm thick Al film is used as the reflective layer, and tantalum pentoxide (Ta_2O_5) with high refractive index of ≈ 2.2 is used as both the dielectric layer (#4) and AR layer (#2). For the blue color filter, the thickness of the Ta_2O_5 for layer #4 is fixed at $d_4 = 80$ nm, corresponding to the half-wave optical thickness of $\lambda_c = 410$ nm (for blue) and the thickness of the top Ta_2O_5 as AR layer is fixed at $d_2 = 68$ nm corresponding to a quarter-wave optical thickness of $\lambda_0 = 600$ nm (for suppressing red). The ideal n and k of the absorber layers in the region with suppressed reflection (i.e., from 500 to 700 nm for the blue device) at a fixed thickness d can be calculated by setting the overall reflection coefficient r equal to zero

$$r = \frac{r_{12} + r_{2345} e^{2i\beta_2}}{1 + r_{12} r_{2345} e^{2i\beta_2}} = 0 \quad (1)$$

where $r_{12} = \frac{m_1 - m_2}{m_1 + m_2}$, $m_p = n_p + ik_p$ is the complex refractive

index of layer p , $\beta_2 = 2\pi n_2 d_2 / \lambda$, r_{2345} is the total reflection coefficient at the 2–3 interface and directly related to the parameters (n, k, d) of the absorber layer (see the expression of r_{2345} in the Supporting Information).^[43] Figure 1b displays the calculated ideal complex refractive indices (n, k) that satisfy Equation (1) with the absorber layer thickness of $d = 12, 16,$ and 20 nm, respectively. It can be clearly seen that the ideal n and k can be effectively adjusted by changing the thickness of the absorber layer. The values of the ideal n and k gradually decrease when increasing the thickness d from 12 to 20 nm. When the thickness $d = 16$ nm, the complex refractive indices (n, k) of the metal nickel (Ni) and tungsten (W) in the wavelength region from 500 to 700 nm are close to the ideal (n, k). However, as shown in Figure 1c,d, n for Ni is lower than the ideal n and W has higher n value than the ideal n , although the k values of both Ni and W match well with the ideal k . Guided by the calculated ideal n and k , we designed a bilayer absorber consisting of 8 nm Ni and 8 nm W, which can be regarded as an effective absorbing medium that exhibits a better matching with the ideal n and k . The effective n and k of the bilayer absorber can be derived by a simplified analytical expression for the effective permittivity ϵ_{eff} of two ultrathin lossy films

$$\epsilon_{\text{eff}} = \frac{t_1}{t_1 + t_2} \cdot \epsilon_1 + \frac{t_2}{t_1 + t_2} \cdot \epsilon_2 \quad (2)$$

where t_1 and t_2 are the thickness of lossy medium #1 and lossy medium #2, respectively. ϵ_1 and ϵ_2 represent the permittivity of lossy medium #1 and lossy medium #2, respectively.^[44] Note that an alloy of two metals can also be used rather than bilayer structure, and, in fact, is expected to behave more like an effective medium. We summarize two guidelines to produce reflective color filters with high color purity: high reflectivity at the wavelengths of the target colors can be guaranteed by locating the absorber layer at $E(\lambda_c) = 0$; suppressed reflection elsewhere achieved by using the effective medium comprised of two ultrathin lossy films to obtain the zero reflectivity. The high-purity red and green reflective color filters can also be achieved by this general strategy presented above (see more details in Figures S1 and S2, Supporting Information).

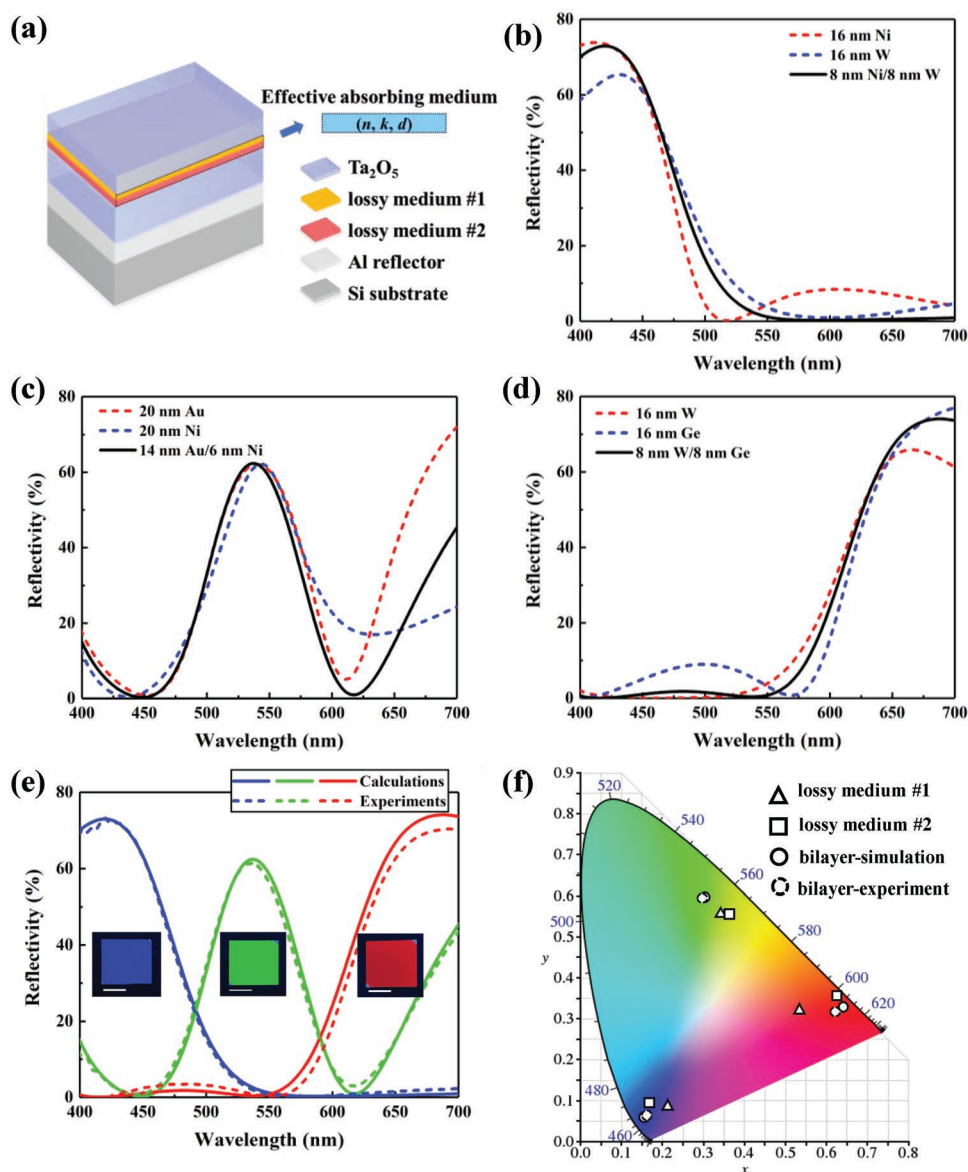


Figure 2. a) A schematic view of the proposed high-color-purity RGB reflective color filters using bilayer absorbers. Two ultrathin lossy films (lossy medium #1 and lossy medium #2) can be regarded as an effective absorbing medium with the complex refractive index (n, k) and the total thickness d . b–d) Comparison of the simulated reflection spectra of RGB color filters employing single lossy medium #1, lossy medium #2, and the corresponding bilayer as the absorber layer. e) The simulated and measured reflection spectra of the proposed RGB color filters based on bilayer absorbers at normal incidence. Insets show the optical images of fabricated RGB devices on silicon substrates (scale bars: 1.0 cm). f) The calculated chromaticity coordinates corresponding to all the reflection spectra shown in (b)–(e) in the CIE 1931 chromaticity diagram.

Figure 2a schematically depicts the proposed bilayer absorber-based reflective color filters featuring high color purity, high brightness, and good angle insensitivity. In the device structure, the combination of lossy medium #1 and lossy medium #2 can be regarded as an effective absorbing medium with the effective complex refractive index of (n, k) and the total thickness of d . Different RGB color filters can be realized by adjusting the thicknesses of the top and middle Ta_2O_5 layers, and designing suitable effective absorbing media. The detailed structure configuration of each color is summarized in **Table 1**. It is worth noting that a much thicker dielectric

layer (one wavelength optical thickness of λ_c) is chosen for the green color filter design to create the second-order F–P cavity resonance mode, achieving narrower reflection peak and better color purity. Besides, the thickness of the AR layer in the green color filter is fixed to the one-eighth wavelength optical thickness of λ_0 , which is attributed to the nontrivial reflection phase shift (i.e., not 0 or π) at the interface between the AR layer and the absorber layer (see more details in Figure S3, Supporting Information). In order to verify the function of effective absorbing medium design, we compared the simulated reflection spectra of color filters employing single lossy

Table 1. Structural configurations of the high-purity RGB reflective color filters. 100 nm thick Al is employed as the bottom reflection mirrors in all designs.

	Top Ta ₂ O ₅	Medium #1	Medium #2	Middle Ta ₂ O ₅
Red	44 nm	8 nm W	8 nm Ge	130 nm
Green	26 nm	14 nm Au	6 nm Ni	228 nm
Blue	68 nm	8 nm Ni	8 nm W	80 nm

medium #1 (the red dashed curves), lossy medium #2 (the blue dashed curves), and the corresponding bilayer absorbers (the black solid curves) at normal incidence for all the three colors as illustrated in Figure 2b–d. The proposed RGB color filters based on bilayer absorbers create the optical responses with the reflection peaks at the wavelengths of 688, 538, and 420 nm and the reflection intensities of 74%, 63%, and 73%, respectively. More importantly, light absorption in the compliment wavelength range of low reflection (500–700 nm for blue color filter, 400–600 nm for red color filter, and 400–500 nm and 600–700 nm for green color filter) is significantly enhanced by using the effective medium absorbers for all three colors compared with those using single absorber layers. Figure 2e plots the reflection spectra (dashed lines) of the fabricated RGB color filters based on bilayer absorbers design measured at normal incidence, presenting a good agreement with the simulated profiles (solid lines). The slight discrepancy is due to the thickness variation in the fabrication process. The optical images of the fabricated samples are inserted in Figure 2e, showing large-area blue, green, and red color filters with high saturation and brightness. The corresponding color coordinates are evaluated from the calculated and the measured reflection spectra and described on the CIE 1931 chromaticity diagram in Figure 2f. The bilayer absorber-based color filters exhibit much improved color purity compared to the devices using only a single absorber layer. Moreover, the color coordinates of both the simulated (red (0.640, 0.330), green (0.303, 0.600), and blue (0.151, 0.062)) and measured (red (0.620, 0.313), green (0.307, 0.592), and blue (0.153, 0.062)) results are very close to the standard RGB (red (0.64, 0.33), green (0.3, 0.6), and blue (0.15, 0.06)) utilized in liquid crystal displays. The detailed color coordinates of all the spectra are summarized in Table S1 (Supporting Information). It should be noted that the deposited Ta₂O₅ is slightly lossy, so the brightness of the designed color filters can be further improved by replacing Ta₂O₅ by a lossless dielectric material. For example, highly pure green color filter with the maximum reflectivity surpassing 80% has been experimentally achieved by using the titanium (Ti)/copper (Cu) bilayer film as the absorber layer and adopting TiO₂ as the dielectric layer and the AR layer (see more details in Figure S4, Supporting Information). According to the reflection spectra comparisons in Figure S5 in the Supporting Information, the RGB color filters using ultrathin effective medium absorbers also exhibit much higher color purity than single lossy medium based color filters in the case of the other two absorber layer thicknesses ($d = 12$ and 20 nm for red and blue colors; $d = 12$ and 16 nm for green colors). The complex refractive indices of all the materials used for the simulations are depicted in Figure S6 (Supporting Information). In addition, all the reflection spectra of RGB color

filters after exchanging the positions of lossy medium #1 and lossy medium #2 or employing the corresponding effective absorbing media match very well with that of the proposed high-purity RGB color filters, further validating the applicability of effective medium theory for the absorber design, as shown and discussed in Figure S7 (Supporting Information). Therefore, the effective absorbing medium design provides an additional freedom to design the high purity RGB reflective colors by searching for suitable bilayer absorbers to satisfy the ideal (n , k) of the absorber layer at a given thickness. In principle, the presented guidelines can be used to design a wide range of thin-film structural color filters with high color purity and brightness in the visible or other wavelength regions.

In order to gain further insight into the strong optical interference performance in this multilayer film structure, we calculated the normalized intensity distributions of electric field inside the whole structures of the designed RGB colors as a function of the wavelength as displayed in Figure 3a–c. Taking the blue colored device for example, strong electric field in the Ni/W bilayer absorber appears at wavelength >500 nm, directly resulting in the efficient light absorption beyond the blue color range. The electric field intensities in the Ni/W bilayer film are very weak in the short wavelength range <500 nm, ensuring minimum loss for blue reflection. Therefore, the electric field distribution in the absorber layer as a function of the wavelength matches well with the optical response of the blue color filter in Figure 2e. Similarly, the enhanced electric field in the wavelength ranges of nontarget colors can also be observed in the absorber layers for the green and red color devices as highlighted by the black dotted zones in Figure 3b,c. The net phase shifts in the top and the middle Ta₂O₅ resonant cavities at different wavelengths for these three devices are also calculated and plotted in Figure 3d–f to reveal the resonant locations. Essentially, the cavity resonances occur when the net phase shift is equal to a multiple of 2π , where the net phase shift includes two reflection phases acquired upon reflection from both the top and bottom interfaces and the propagation phase accumulated within the layer. As illustrated by the red solid curves in Figure 3d–f, fundamental F–P cavity resonance modes are excited within the middle Ta₂O₅ dielectric layers for the blue (@460 nm) and red (@621 nm) colors, while the second-order F–P cavity resonance is excited at 568 nm for the green color to ensure narrower bandwidth of the reflection spectrum. Obviously, F–P cavity resonant wavelengths match very well with the locations of the confined electric field inside the middle Ta₂O₅ layers for these three devices. As displayed by the black solid curves in Figure 3d, the AR resonance occurring @635 nm, where the net phase shift of the top Ta₂O₅ is equal to 0, corresponds exactly to the reflection valley in Figure 2e for the blue color. The AR resonance is the direct reason for the enhanced electric field inside the absorber layer within the wavelength range highlighted in Figure 3a, which suppresses the reflection at off-peak wavelengths. Figure S8 in the Supporting Information compares the reflection spectra of the blue color filter with and without the top Ta₂O₅ overlayer, validating the AR function of the top Ta₂O₅ overlayer outside the blue color range. For the green color shown in Figure 3e, two closely positioned AR resonances (@418 nm and @ 464 nm) are excited within the top

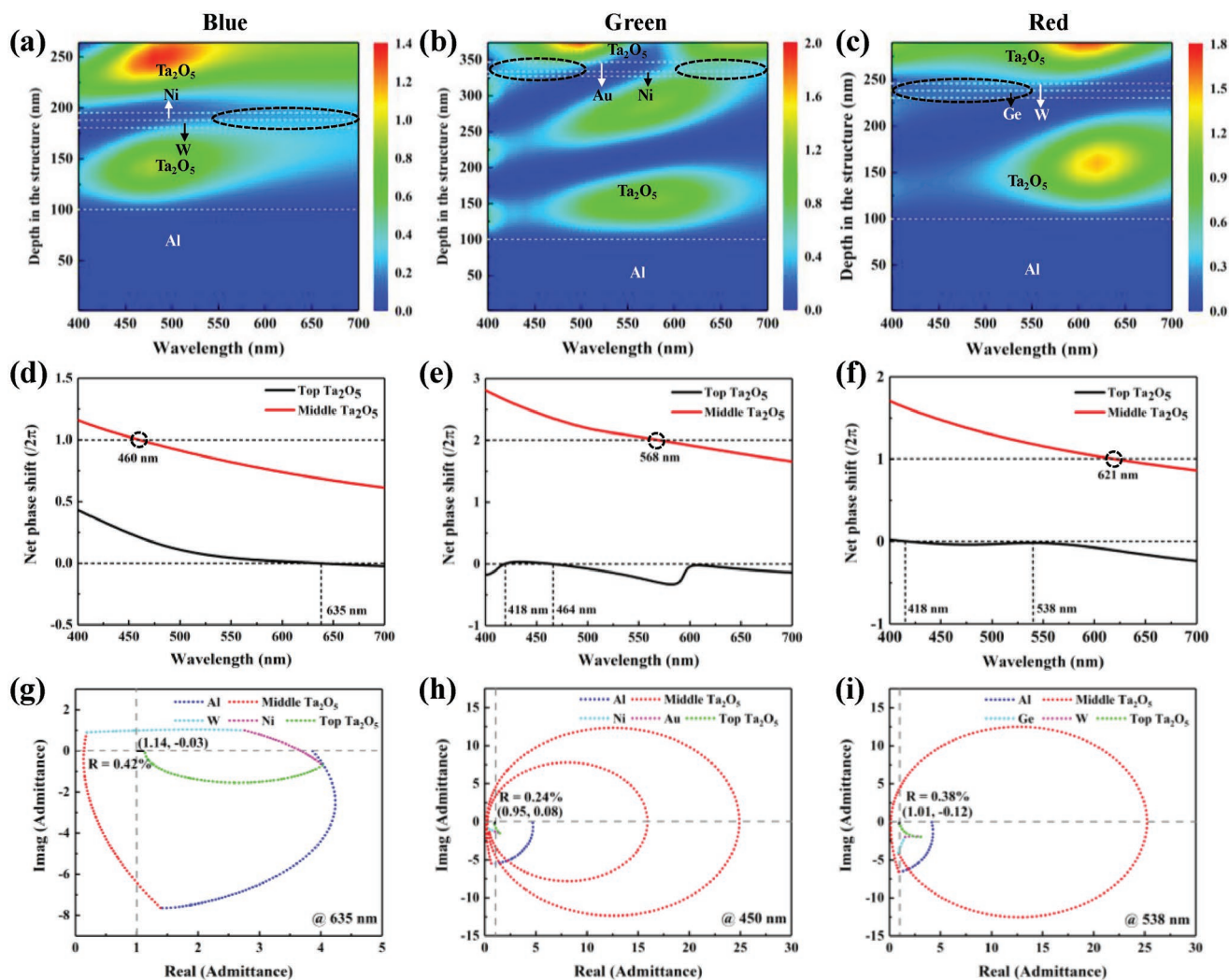


Figure 3. a–c) The wavelength-dependent electric field distributions inside the whole structures of the proposed RGB color filters. d–f) Calculated total phase shifts in the top and middle Ta₂O₅ layers as a function of the wavelength for these three devices. g–i) Optical admittance diagrams of the proposed RGB color filters at the wavelengths of absorption peak. The distance from the final admittance point to the air (1, 0) represents how high reflection is at normal incidence.

Ta₂O₅ layer. These two resonances overlap together to create a perfect absorption peak at 450 nm. For the red color shown in Figure 3f, the AR resonances occur @418 nm and @538 nm, matching very well with the positions of two reflection valleys in the reflection spectrum. In order to further validate the strong absorption performance at off-peak wavelengths resulting from the AR resonances, the optical admittance diagrams from the proposed RGB reflective color filters at the wavelengths of absorption peak are plotted in Figure 3g–i. The optical admittance ($Y = \sqrt{\epsilon/\mu}$) is the inverse of the impedance, with ϵ and μ being the permittivity and permeability, respectively, and numerically equal to the material complex refractive index because the relative permeability of typical materials remains unity at optical frequencies.^[39,45] The admittance of the entire structure starts from the silicon substrate and rotates on a circular or spiral trajectory depending on the both the thickness and the optical constant of the material. The distance between the termination admittance point of the

layered structure and the admittance of air (1, 0) determines the reflectivity by

$$R = \left(\frac{1 - (x + iy)}{1 + (x + iy)} \right)^2 \quad (3)$$

where x and y are the real and imaginary parts of the final admittance. Calculated coordinates of the final admittance at the corresponding wavelengths of absorption peak are (1.14, -0.03), (0.95, 0.08), and (1.01, -0.12) for blue, green, and red colors, respectively. These admittance points are very close to that of the air, resulting in the significantly suppressed reflections of less than 1%, as can be seen from the calculated reflectivity values.

To validate the angular performance of the proposed RGB reflective color filters based on ultrathin bilayer absorbers, we simulated and measured their angle-resolved reflection spectra under unpolarized light illumination, as shown in

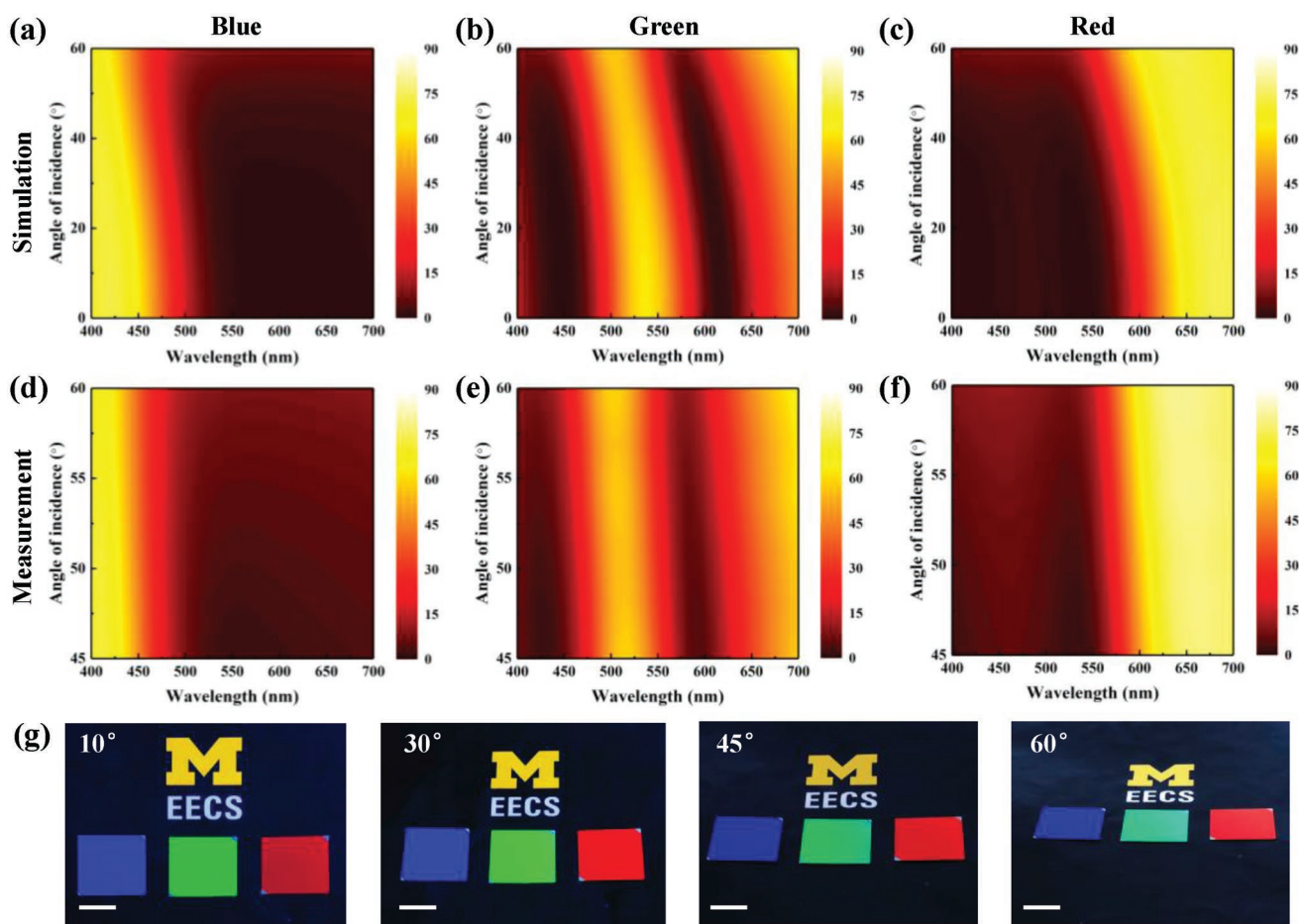


Figure 4. a–c) The simulated and d–f) measured angle-resolved reflection spectra of the proposed RGB reflective colors based on bilayer absorbers under unpolarized light incidence. g) Photographic images of the fabricated samples taken at oblique incidence of 10°, 30°, 45°, and 60°. The scale bars are 1.0 cm.

Figure 4a–c and d–f, respectively. It is clear that the simulation results are very consistent with the corresponding experimental results for all the three colors, showing the relatively flat dispersion curves despite the slight blue shifts of the resonant wavelengths when the incident angle increases from 0° to 60°. The photographs of the fabricated devices taken at different observation angles are shown in Figure 4g and the color change with the incident angle up to 60° is also displayed on the CIE 1931 chromaticity diagram in Figure S9 in the Supporting Information. Obviously, the stable color appearances and the closely located color coordinates at different incident angles prove the high angular tolerance up to $\pm 60^\circ$ for blue and red colors. Due to the thicker Ta₂O₅ dielectric layer used in the green color filter, its angle-invariant appearance can only be maintained up to $\pm 45^\circ$. It should be noted that the angle-independent property of the DADM thin-film color filters proposed here can be further improved by using dielectric materials with even higher refractive index, such as ZnS ($n \approx 2.6$), instead of Ta₂O₅ as the spacer layer, or adding additional phase compensating overlayers.

3. Conclusions

In summary, we present a general strategy for the material and layer thickness selection to produce bright and high-purity reflective colors in a classic asymmetric F–P cavity structure consisting of an anti-reflection overlayer, an absorber layer, a spacer layer, and a reflective mirror. Guided by the calculated complex refractive index of the absorber layer to achieve near-ideal absorption, an effective absorbing medium comprised of two ultrathin lossy films is designed to enhance the optical absorption over a broad wavelength range of nontargeted colors, thus significantly improving the color purity of the desired reflective colors. To prove the power and simplicity of this strategy, we demonstrated in theory and experiment high-purity RGB reflective color filters with good angular tolerance (blue and red colors are up to $\pm 60^\circ$ and green color is up to $\pm 45^\circ$) by exploiting W/Ge, Au/Ni, and Ni/W bilayer absorbers, respectively, to function as effective absorber media. Compared with previous studies, the generalized design principles and the proposed method of searching for suitable effective bilayer absorbers open up new avenues for achieving high-purity thin-film structural colors

with more materials selections. Moreover, the fabrication process of the whole structure only involves simple thin-film deposition technologies, thereby enabling their great potential toward large-scale applications in various areas.

4. Experimental Section

Device Fabrication: All the designed RGB reflective color filters were fabricated by using an electron beam (E-beam) evaporator and a sputtering system (LAB 18, Kurt J. Lesker Company) on silicon substrates at room temperature. Au, Ni, and W films were deposited with direct current (DC) sputtering at the rate of 8.6, 5.1, and 3.6 Å s⁻¹, respectively, while Ta₂O₅ was sputtered with radio frequency (RF) sputtering at the rate of 0.5 Å s⁻¹. All the sputtering processes were carried out under the argon pressure of 3 × 10⁻⁶ Torr. Al, Ge, Cu, Ti, and TiO₂ films were deposited at the rate of 3 Å s⁻¹ when the pressure of the E-beam evaporator chamber was prepumped down to 4 × 10⁻⁶ Torr.

Simulation and Measurements: The transfer matrix method was used to simulate the reflection spectra, phase information, and normalized electric field distributions. The reflection spectra under unpolarized light incidence were calculated by taking the average of the results of TE and TM polarizations. A thin-film measurement instrument (F20, Filmetrics) was used to measure the reflection spectra of the proposed RGB color filters at normal incidence. The measured angle-resolved reflection spectra were attained using a spectroscopic ellipsometer (M-2000, J. A. Woollam). The same ellipsometer was applied to extract the refractive indices of all the materials used in the optical simulations.

Supporting Information

Supporting Information is available from the Wiley Online Library or from the author.

Acknowledgements

Z.Y. and C.J. contributed equally to this work. Z.Y. acknowledges support from the International Postdoctoral Exchange Fellowship Program (No. 20170094) and from Inlight Tech. Ltd. C.J. acknowledges a Rackham Research grant from the University of Michigan. D.L. acknowledges support from the National Natural Science Foundation of China (No. 51606099) and the Natural Science Foundation of Jiangsu Province (No. BK20160838).

Conflict of Interest

L.J.G. declares financial interest to this work.

Keywords

effective absorbing medium, Fabry–Pérot cavity, interference effect, reflective color filters, ultrathin lossy films

Received: May 3, 2019

Revised: June 29, 2019

Published online: September 2, 2019

- [1] X. Y. Duan, S. Kamin, N. Liu, *Nat. Commun.* **2017**, *8*, 14606.
 [2] Y. S. Wang, M. J. Zheng, Q. F. Ruan, Y. M. Zhou, Y. Q. Chen, P. Dai, Z. M. Zhang, Z. H. Lin, Y. X. Long, Y. Li, N. Liu, C. W. Qiu, J. K. W. Yang, H. G. Duan, *Research* **2018**, *2018*, 8109054.

- [3] L. Shao, X. L. Zhuo, J. F. Wang, *Adv. Mater.* **2018**, *30*, 1704338.
 [4] A. V. Yakovlev, V. A. Milichko, V. V. Vinogradov, A. V. Vinogradov, *ACS Nano* **2016**, *10*, 3078.
 [5] Z. M. Yang, Y. Q. Chen, Y. M. Zhou, Y. S. Wang, P. Dai, X. P. Zhu, H. G. Duan, *Adv. Opt. Mater.* **2017**, *5*, 1700029.
 [6] F. Cheng, J. Gao, T. S. Luk, X. D. Yang, *Sci. Rep.* **2015**, *5*, 11045.
 [7] J. Hong, E. Chan, T. Chang, T. C. Fung, B. Hong, C. Kim, J. Ma, Y. L. Pan, R. V. Lier, S. G. Wang, B. Wen, L. X. Zhou, *Optica* **2015**, *2*, 589.
 [8] S. Koyama, Y. Inaba, M. Kasano, T. Murata, *IEEE Trans. Electron Devices* **2008**, *55*, 754.
 [9] S. Yokogawa, S. P. Burgos, H. A. Atwater, *Nano Lett.* **2012**, *12*, 4349.
 [10] W. Yuan, N. Zhou, L. Shi, K. Q. Zhang, *ACS Appl. Mater. Interfaces* **2015**, *7*, 14064.
 [11] H. J. Park, T. Xu, J. Y. Lee, A. Ledbetter, L. J. Guo, *ACS Nano* **2011**, *5*, 7055.
 [12] K. T. Lee, J. Y. Lee, S. Y. Seo, L. J. Guo, *Light: Sci. Appl.* **2014**, *3*, e215.
 [13] Y. C. Shen, C. W. Hsu, Y. X. Yeng, J. D. Joannopoulos, M. Soljacic, *Appl. Phys. Rev.* **2016**, *3*, 011103.
 [14] S. Sadreddin Mirshafieyan, J. P. Guo, *Opt. Express* **2014**, *22*, 31545.
 [15] A. S. Roberts, A. Pors, O. Albrektsen, S. I. Bozhevolnyi, *Nano Lett.* **2014**, *14*, 783.
 [16] M. L. Tseng, J. Yang, M. Semmlinger, C. Zhang, P. Nordlander, N. J. Halas, *Nano Lett.* **2017**, *17*, 6034.
 [17] V. Flauraud, M. Reyes, R. Paniagua-Dominguez, A. I. Kuznetsov, J. Brugger, *ACS Photonics* **2017**, *4*, 1913.
 [18] S. Sun, W. H. Yang, C. Zhang, J. X. Jing, Y. S. Gao, X. Y. Yu, Q. H. Song, S. M. Xiao, *ACS Nano* **2018**, *12*, 2151.
 [19] Z. G. Dong, J. F. Ho, Y. F. Yu, Y. H. Fu, R. Paniagua-Dominguez, S. H. Wang, A. I. Kuznetsov, J. K. W. Yang, *Nano Lett.* **2017**, *17*, 7620.
 [20] A. F. Kaplan, T. Xu, L. J. Guo, *Appl. Phys. Lett.* **2011**, *99*, 143111.
 [21] C. T. Wang, H. H. Hou, P. C. Chang, C. C. Li, H. C. Jau, Y. J. Hung, T. H. Lin, *Opt. Express* **2016**, *24*, 22892.
 [22] B. Yang, W. W. Liu, Z. C. Li, H. Cheng, S. Q. Chen, J. G. Tian, *Adv. Opt. Mater.* **2018**, *6*, 1701009.
 [23] X. L. Zhu, W. Yan, U. Levy, N. A. Mortensen, A. Kristensen, *Sci. Adv.* **2017**, *3*, e1602487.
 [24] T. Lee, J. Jang, H. Jeong, J. Rho, *Nano Converg.* **2018**, *5*, 1.
 [25] S. J. Tan, L. Zhang, D. Zhu, X. M. Goh, Y. M. Wang, K. Kumar, C. W. Qiu, J. K. W. Yang, *Nano Lett.* **2014**, *14*, 4023.
 [26] S. Sun, Z. X. Zhou, C. Zhang, Y. S. Gao, Z. H. Duan, S. M. Xiao, Q. H. Song, *ACS Nano* **2017**, *11*, 4445.
 [27] M. J. Uddin, R. Magnusson, *Opt. Express* **2013**, *21*, 12495.
 [28] Z. Y. Li, S. Butun, K. Aydin, *ACS Photonics* **2015**, *2*, 183.
 [29] C. S. Park, V. R. Shrestha, S. S. Lee, D. Y. Choi, *Sci. Rep.* **2016**, *6*, 25496.
 [30] Z. M. Yang, Y. M. Zhou, Y. Q. Chen, Y. S. Wang, P. Dai, Z. G. Zhang, H. G. Duan, *Adv. Opt. Mater.* **2016**, *4*, 1196.
 [31] C. S. Park, V. R. Shrestha, S. S. Lee, E. S. Kim, D. Y. Choi, *Sci. Rep.* **2015**, *5*, 8467.
 [32] C. Y. Yang, K. N. Mao, W. D. Shen, B. Fang, X. Fang, X. Zhang, Y. G. Zhang, X. Liu, *Appl. Phys. Lett.* **2016**, *109*, 241104.
 [33] M. A. Kats, R. Blanchard, P. Genevet, F. Capasso, *Nat. Mater.* **2013**, *12*, 20.
 [34] K. T. Lee, S. Seo, J. Y. Lee, L. J. Guo, *Adv. Mater.* **2014**, *26*, 6324.
 [35] H. X. Deng, Z. G. Li, L. Stan, D. Rosenmann, D. Czaplowski, J. Gao, X. D. Yang, *Opt. Lett.* **2015**, *40*, 2592.
 [36] C. G. Ji, C. Y. Yang, W. D. Shen, K. T. Lee, Y. G. Zhang, X. Liu, L. J. Guo, *Nano Res.* **2019**, *12*, 543.
 [37] K. T. Lee, J. Y. Jang, S. J. Park, C. G. Ji, S. M. Yang, L. J. Guo, H. J. Park, *Adv. Opt. Mater.* **2016**, *4*, 1696.

- [38] K. T. Lee, S. Y. Han, H. J. Park, *Adv. Opt. Mater.* **2017**, *5*, 1700284.
- [39] C. G. Ji, K. T. Lee, L. J. Guo, *Opt. Lett.* **2019**, *44*, 86.
- [40] C. Y. Yang, W. D. Shen, Y. G. Zhang, K. Li, X. Fang, X. Zhang, X. Liu, *Sci. Rep.* **2015**, *5*, 9285.
- [41] D. Banerjee, *US 9658375 B2*, **2017**.
- [42] C. G. Ji, K. T. Lee, T. Xu, J. Zhou, H. J. Park, L. J. Guo, *Adv. Opt. Mater.* **2017**, *5*, 1700368.
- [43] D. Liu, H. T. Yu, Z. Yang, Y. Y. Duan, *Nano Res.* **2016**, *9*, 2354.
- [44] C. Della Giovampaola, N. Engheta, *Nat. Mater.* **2014**, *13*, 1115.
- [45] Y. J. Jen, C. C. Lee, K. H. Lu, C. Y. Jheng, Y. J. Chen, *Opt. Express* **2015**, *23*, 33008.